Fermiology and transport in metallic monatomic layers on semiconductor surfaces

2007 J. Phys.: Condens. Matter 19 355007

(http://iopscience.iop.org/0953-8984/19/35/355007)

IOP PUBLISHING JOURNAL OF PHYSICS: CONDENSED MATTER

J. Phys.: Condens. Matter **19** (2007) 355007 (26pp) doi:10.1088/0953-8984/19/35/355007

Fermiology and transport in metallic monatomic layers on semiconductor surfaces

Iwao Matsuda[1] **and Shuji Hasegawa**[2]

[1] Synchrotron Radiation Laboratory, The Institute for Solid State Physics, The University of Tokyo, 5-1-5 Kashiwa-no-ha, Kashiwa, Chiba 277-8581, Japan
[2] Department of Physics, School of Science, The University of Tokyo, 7-3-1 Hongo, Bunkyo-ku, Tokyo 113-0033, Japan

E-mail: imatsuda@issp.s.u-tokyo.ac.jp

Received 5 April 2007, in final form 6 April 2007
Published 20 August 2007
Online at stacks.iop.org/JPhysCM/19/355007

Abstract

We review Fermi surfaces and band dispersion of metallic monatomic layers (surface superstructures) on semiconductor substrates studied by photoemission spectroscopy, in connection with the surface electronic transport properties. By using various surface superstructures such as two- and quasi-one-dimensional metallic ones, the conductivity, its anisotropy, and the Hall effect in the surface states are understood quantitatively by the Fermi surfaces and band dispersion using the Boltzmann picture. The experimental techniques and analysis procedures are described, which are applicable to various surface systems. This demonstrates that surface atomic layers provide an intriguing platform for the study of atomic-scale low dimensional electron dynamics.

(Some figures in this article are in colour only in the electronic version)

1. Introduction

The shape and size of the Fermi surface of a metal govern various physical properties such as electronic transport, magnetic/optical properties, and phase transitions such as the Peierls transition [1–8]. Studies on Fermi surfaces, so-called Fermiology, have started since the middle of the 20th century through research on oscillatory galvanomagnetic effects: the de Haas–van Alphen and the Shubnikov–de Haas effects have become powerful tools to determine the shape of Fermi surfaces [7–9]. However, the measurements require quite extreme experimental conditions, such as high magnetic fields ($\geqslant$1 T) and low temperatures ($\leqslant$10 K). Other probes for Fermi surfaces are also developed, utilizing, e.g., Compton scattering and positron annihilation [10]. These techniques do not require extreme experimental conditions, but their resolutions in **k**-space are quite limited.

Angle-resolved photoemission spectroscopy (ARPES) has become one of the most powerful probes for Fermi surface mapping [4, 5]. It enables one to determine the valence

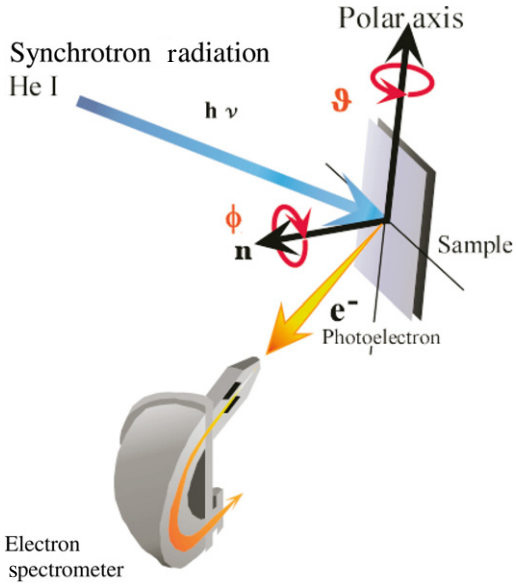

Figure 1. An experimental set-up for the photoemission Fermi surface and band dispersion mapping. With a fixed arrangement of photon source (He lamp or synchrotron radiation) and an electron spectrometer, photoelectrons from a sample are detected at various polar (ϑ) and azimuth angles (ϕ) by rotating and tilting the sample.

band dispersion through acquiring energy spectra at various polar and azimuth angles with a small acceptance-angle detector. The experimental set-up is schematically drawn in figure 1. The sensitivity from surface to volume is tuned by choosing appropriate photon energy [5, 11]. If the ARPES scan is performed by setting the detection energy window at a small interval around the Fermi level (E_F), the Fermi surface is mapped out by accumulating the data over a wide range of emission angles (wavevector, **k** space). In this way, the Fermi surface of a one-dimensional (1D) or two-dimensional (2D) metal can be determined directly and, for a three-dimensional (3D) metal, sections through the Fermi surface can be obtained.

Research on atomic layers or surface superstructures on crystal surfaces have been triggered by interest in studying their physical properties, that are quite different from well known 3D bulk crystals [12]. Nowadays, surface systems have become an important playground for low dimensional physics [13, 16, 17, 19]. This is because the atomic structures of surfaces can be directly observed by various surface science techniques such as scanning probe microscopes and electron (positron) diffractions [12, 20, 21]. Furthermore, since photoelectrons excited by vacuum ultraviolet (VUV) light, conventional photons for photoemission spectroscopy, originate mostly from surface layers due to very short electron escape depth, we can routinely probe the surface electronic states [5]. On clean or metal-covered surfaces, various 1D or 2D metal structures are formed. While an isotropic free-electron system in 3D possesses a Fermi sphere (figure 2(a)), that in 2D has a Fermi cylinder (figures 2(b) for isotropic and (c) for anisotropic cases), and that in (quasi-)1D is Fermi sheets (figures 2(d) and (e)). The Fermi contours in various dimensions are schematically depicted in figure 2. In 2D (on a k_x–k_y plane), figures 2(b) and (c) correspond to Fermi circles and hexagons, respectively, while figures 2(d) and (e) are Fermi lines.

Such Fermi surfaces of various metallic surface superstructures have been recognized directly by ARPES measurements as shown in figure 3. Figure 3(a) is a quasi-1D Fermi

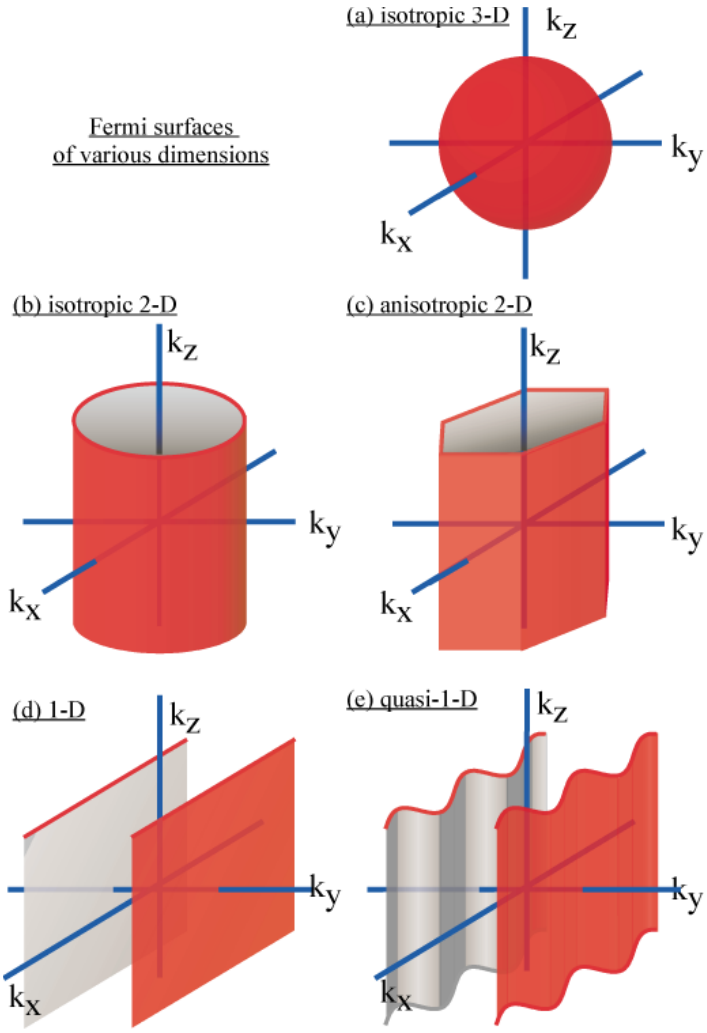

Figure 2. Fermi surfaces in various dimensions. (a) Isotropic three-dimensional (3D) sphere, (b) isotropic two-dimensional (2D) cylinder, (c) anisotropic (hexagonal) 2D cylinder, (d) one-dimensional (1D) sheet, and (e) quasi-1D sheet.

surface of the Si(111)4 × 1-In surface [22]. The Fermi surface is actually wavy sheets as shown in figure 2(e), and satisfies the nesting condition, leading to a Peierls phase transition. Figure 3(b) is circular Fermi surfaces of sub-bands of isotropic 2D quantum-well states formed in a ultrathin Ag film prepared on Si(111)7 × 7 [23, 24]. Figures 3(c) and (d) are hexagonal Fermi surfaces for Ge(111)$\sqrt{3} \times \sqrt{3}$-Sn [25] and 'discommensurate' Si(111)$''$5.55 × 5.55$''$-Cu [26], respectively. Figure 3(e) is Fermi surfaces of an ultrathin Bi film on Si(111)7 × 7, showing a hexagonal hole pocket around the $\overline{\Gamma}$ point ($k_x = k_y = 0$) and surrounding six oval electron pockets [27]. Relations between such hexagonal Fermi surfaces and charge-density-wave transitions have been one of the central issues in surface science.

Electrons at E_F (on the Fermi surface) are in general responsible for transport phenomena. Transport through surface states is also the case, which has now been an important issue for studying atomic-scale low dimensional electron dynamics. A relation between the

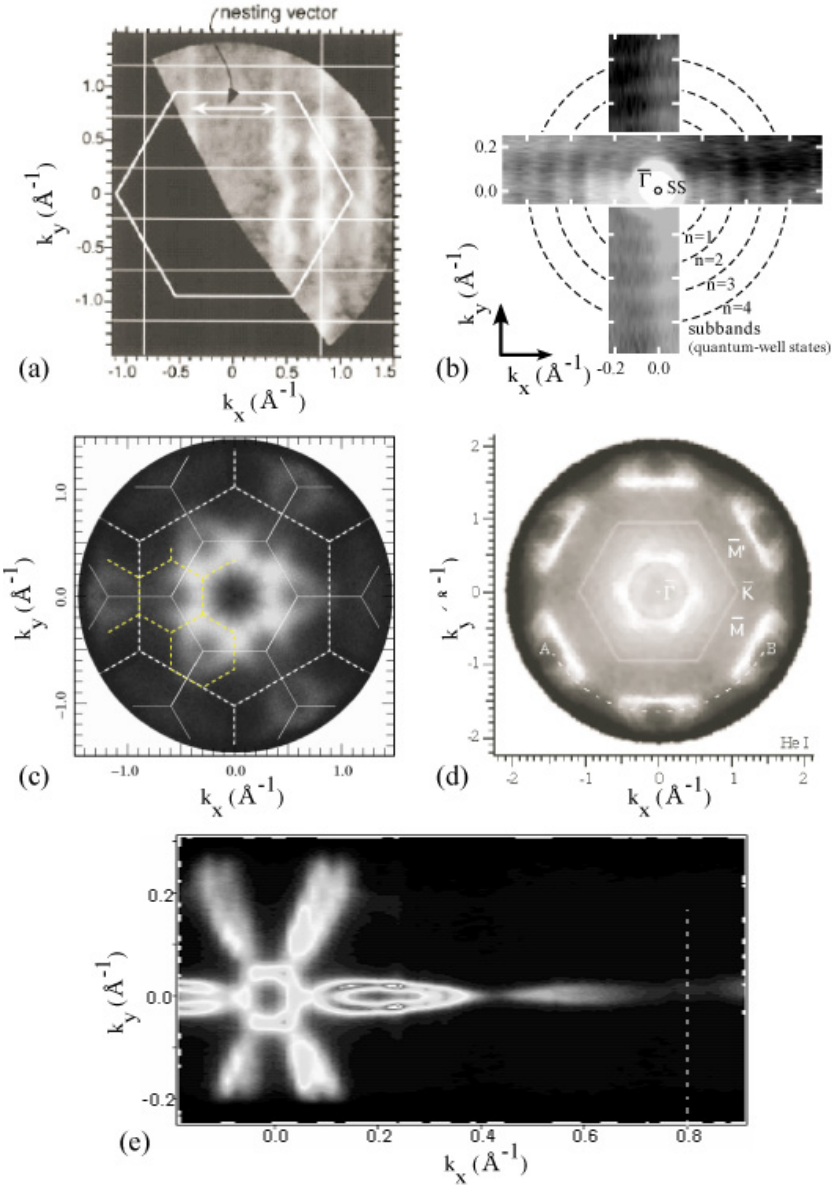

Figure 3. Photoemission Fermi surfaces of various surface superstructures and quantum films on semiconductor substrates. (a) Si(111)4 × 1-In taken with a 137 mm Perkin–Elmer Omni IV spectrometer [22]. (b) Quantum Ag(111) film with a Gammadata-Scienta SES-100 [23]. (c) Ge(111)$\sqrt{3} \times \sqrt{3}$-Sn with VG ADES-400 [25]. (d) Discommensurate Si(111)'5.55 × 5.55'-Cu with VG ESCALAB 220 [26]. (e) Quantum Bi(111) film with a Gammadata-Scienta SES-100 [27].

conductivity and the Fermi surface is derived from the Boltzmann equation as follows, with an approximation that the carrier relaxation time τ is independent of the electron wavevector [28]. The conductivity tensor is given by

$$\sigma_{ij} = \frac{e^2\tau}{2\pi^2\hbar} \int \frac{v_{ki}\, v_{kj}\, \mathrm{d}k_\mathrm{F}}{|v_k|}, \tag{1}$$

where k_F and v_{ki} are the Fermi wavevector and Fermi velocity vector along the i direction, the latter being obtained from the band dispersion at E_F, $v_k = \nabla_k E_k/\hbar$. The integral is done on the Fermi surface. For the isotropic 2D electronic systems, the formula is reduced to a simple one as [29]

$$\sigma = \frac{e^2}{2} \cdot (\tau \cdot v_F) \cdot v_F \cdot \mathcal{D}^{2D}, \tag{2}$$

where v_F is the Fermi velocity, and $\mathcal{D}^{2D}$ the 2D density of states at E_F. The product $(\tau \cdot v_F)$ is the mean free path ℓ of Fermi electrons. The conductivity is thus reasonably expressed by a product of the mean free path, velocity and concentration of Fermi electrons. These quantities are basically derived by the electronic states only at E_F, which is directly given by photoemission measurements.

Monatomic layers on crystal surfaces are not only interesting for condensed matter physics, but also have important possibilities for applications to solid devices. Rapid progress in the miniaturization of microelectronic devices now forces the signal currents to flow near the surface/interface region in semiconductor crystals and ultimately through only one atomic layer. Despite such scientific and technological interests, the conductivity measurement of surface atomic layers has been a challenging experiment since the surface inevitably has an electrical contact with the substrate that hampers detection of the intrinsic surface conductivity. Much research has attempted to perform surface-sensitive conductivity measurements with various methods such as using semiconductor-on-insulator wafers or patterned surfaces [30–33]. We have developed four-point probe (FPP) measurement methods done *in situ* in ultrahigh vacuum on various surface superstructures [34, 35, 37–40]. We found through the FPP measurements that simple attachment of electrode probes on a sample surface with probe spacing of cm–mm is enough to extract electrical and Hall conductances of surface states quantitatively if one chooses appropriate surface phases and proper data analyses [14–16, 29, 41]. The FPP method with probe spacing on the micrometre scale turns out to be much more sensitive to the surface [35, 36].

In the present paper, we summarize some of our recent studies on Fermi surfaces of metallic atomic layers on semiconductor surfaces studied by photoemission spectroscopy, in connection with surface transport measurements [29, 40, 41]. We have mapped out Fermi surfaces of 2D and 1D surface superstructures through detailed ARPES measurements. We have, on one hand, performed surface transport measurements with our own experimental techniques and succeeded in obtaining the electrical conductivity, its anisotropy, and the Hall coefficient of the metallic surface superstructures. The transport phenomena are quantitatively described by the 2D Fermi surfaces in the Boltzmann picture. The agreement between the photoemission and conductivity results justifies our experimental techniques and analysis procedures for surface-state transport. The combination with Fermi-surface and band-dispersion mapping by ARPES and conductivity measurements by *in situ* FPP methods provide fruitful results in surface physics.

In the following, we introduce, first, an example of an isotropic 2D metallic monolayer on a semiconductor surface, the Si(111)$\sqrt{3} \times \sqrt{3}$-Ag surface. Through monovalent atom adsorptions on this surface, electrons are doped to the metallic surface-state band, leading to a transition to a new-ordered structure, the $\sqrt{21} \times \sqrt{21}$ phase. This structural transition induces a characteristic evolution of Fermi surface topology [29], and also results in drastic changes in electrical conduction and Hall effect [41]. The changes in transport properties are explained in terms of the Fermi surface evolution by using equations (1) and (2). At the end of the review, we briefly introduce a case of a quasi-1D metallic surface, Si(111)4 $\times$ 1-In. The anisotropic surface conductivity is explained by the quasi-1D Fermi surface [40].

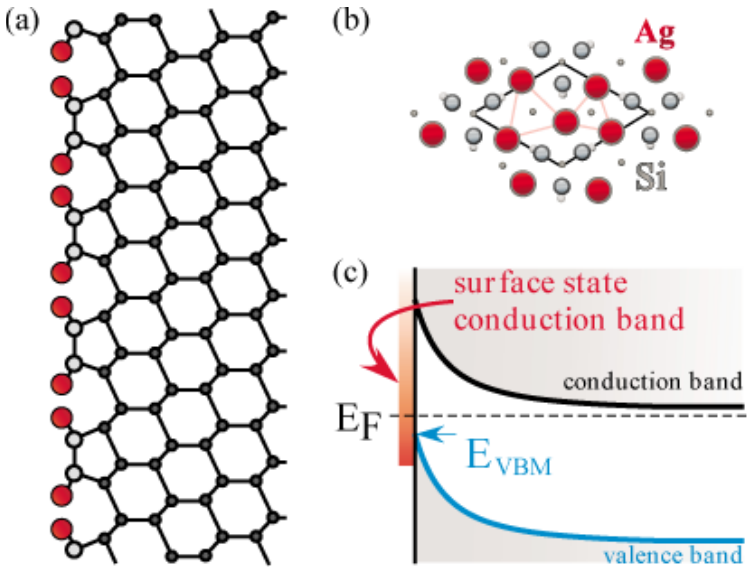

Figure 4. (a) Cross-sectional and (b) plan views of the inequivalent triangle (IET) structural model of Si(111)$\sqrt{3} \times \sqrt{3}$-Ag. The largest (red) circles represent Ag atoms. Other circles are Si atoms. (c) Schematic drawing of the band bending of bulk bands in an n-type substrate below the $\sqrt{3} \times \sqrt{3}$-Ag surface. Vertical and horizontal axes correspond to electron energy and depth from the surface, respectively.

2. Isotropic two-dimensional metal

2.1. Evolution of Fermi surface topology

The Si(111)$\sqrt{3} \times \sqrt{3}$-Ag surface ($\sqrt{3} \times \sqrt{3}$-Ag for short hereafter), induced by one monolayer (ML) Ag adsorption on a Si(111) substrate, has been historically one of the most important prototypes for the metal/semiconductor interface [16, 18, 42–44]. Almost all kinds of surface-science technique have been applied to this surface. Now its atomic and electronic structures are well understood. Figures 4(a) and (b) show cross-sectional and top-view images of the atomic structure model, respectively. This is a so-called 'inequivalent triangle (IET)' model, containing three Ag atoms in the $\sqrt{3} \times \sqrt{3}$ surface unit cell (figure 4(b)) [43, 44]. The Ag atoms form two inequivalent, large and small, triangles in the unit cell. As shown in figure 4(a), only the surface top layer is composed of Ag and Si. The diamond crystal structure of bulk Si is formed below the third layer. However, in the sub-surface region (10 nm–10 μm deep from the surface depending on the doping level in the crystal), the energy position of the valence band maximum (E_{VBM}), referred to E_F, continuously changes from that in the bulk, i.e. band bending, as shown in figure 4(c). This region is a so-called surface space-charge layer. It has been known that E_{VBM} at the $\sqrt{3} \times \sqrt{3}$-Ag surface locates about 0.1 eV below E_F, irrespective of the doping type in the Si substrate [29, 45]. Depending on the doping type in the substrate, therefore, the space-charge layer is classified into an inversion layer (on a n-type substrate) or a hole-accumulation layer (on a p-type substrate) [46]. This is because the sub-surface region below the $\sqrt{3} \times \sqrt{3}$-Ag always accumulates excess holes to compensate the negative charge trapped in the surface states. Another important point from this analysis is that there exists a pn junction between the space-charge layer and the underlying substrate for n-type wafers, resulting in the electrical isolation between the surface region and substrate bulk, while no

barrier is formed on p-type wafers. This is important in the surface conductivity measurements because the measuring current injected from electrodes on the surface does not penetrate into the bulk region due to the pn junction on n-type substrates, while it penetrates deep into the bulk for p-type substrates, making the measurements surface sensitive only for n-type substrates.

Figure 5(a) shows the band dispersion diagram of the $\sqrt{3} \times \sqrt{3}$-Ag surface measured by ARPES. The ARPES results shown in the rest of the paper were acquired with unpolarized He Iα radiation ($h\upsilon = 21.2$ eV), with a commercial Scienta SES-100 angle-resolved photoelectron spectrometer. The Fermi energy was determined by fitting the Fermi edge measured on a Ta holder attached to the sample. In the diagram in figure 5, the intensities of the spectral features, tracing band dispersion curves, are represented by the brightness in grey-scale [24]. The black region near E_F indicates the band gap, semiconducting nature of the bulk Si. Within the bulk band gap, a metallic band crossing E_F locates at $k_x \sim 1.1$ Å^{-1}, which is a surface-state band of $\sqrt{3} \times \sqrt{3}$-Ag. As shown in a magnified image in figure 5(b), the surface-state band has parabolic dispersion around $\overline{\Gamma}_{\sqrt{3}}$ with an effective mass, m^*, of about 0.13 m_0, where m_0 is the free-electron mass [47]. The Fermi surface made by this band is a complete circle around the $\overline{\Gamma}_{\sqrt{3}}$ point as shown in figure 5(d) [48, 49].

When a small amount (<0.1 ML) of noble-metal atoms is deposited on this $\sqrt{3} \times \sqrt{3}$-Ag surface, one can find adatoms and nanoclusters, composed of three adatoms, sparsely and randomly adsorbed on the surface. Figure 6(a) is an STM image of Ag adatoms and Ag nanoclusters on the $\sqrt{3} \times \sqrt{3}$-Ag surface. A periodic protrusion is assigned to the smaller Ag triangle in the IET structure model in figure 4(b) [44]. Similar nanoclusters are also found for the Au deposition, and they distribute on the surface uniformly as shown in figure 6(b) [50]. These adatoms donate electrons to the $\sqrt{3} \times \sqrt{3}$-Ag surface layer. However, the free-electron surface-state band (figure 5(b)) shows non-rigid band behaviour through the electron doping. Figures 6(c)–(e) are grey-scale band dispersion images with Au coverage ranging from 0.01 to 0.03 ML. The binding energy of the band bottom becomes larger with the Au coverage and, at the same time, the surface-state bands show splitting [50]. The adatom-induced band is probably a resonant band and localized states around the nanoclusters, which hybridize with the delocalized $\sqrt{3} \times \sqrt{3}$-Ag surface-state band. Similar changes in electronic band dispersion are also found for alkali-metal deposition on the $\sqrt{3} \times \sqrt{3}$-Ag surface [50].

When the coverage of monovalent atoms such as noble metal (Cu, Ag, Au) and alkali metal (Na, K, Cs) on top of the $\sqrt{3} \times \sqrt{3}$-Ag reaches 0.14 ML, the nanoclusters are arranged periodically and the surface exhibits a phase transition to a $\sqrt{21} \times \sqrt{21}$ phase [16, 29, 42, 51–54]. Figure 7(a) shows STM images of the $\sqrt{3} \times \sqrt{3}$ and $\sqrt{21} \times \sqrt{21}$ phases prepared by additional Ag deposition. In contrast to the simple $\sqrt{3} \times \sqrt{3}$ image, the $\sqrt{21} \times \sqrt{21}$ phase has much more complicated STM features [53]. Concerning the $\sqrt{21} \times \sqrt{21}$ surface structure, various models of atomic arrangement have been proposed, but the structure has still remained controversial. Therefore, there has been no theoretical STM simulation reported for the $\sqrt{21} \times \sqrt{21}$ surface to assign STM features in figure 7(a). Up to now, a structure model with three adatoms per $\sqrt{21} \times \sqrt{21}$ unit cell adsorbed on the $\sqrt{3} \times \sqrt{3}$-Ag substrate has been found to be the most plausible [21, 54].

Figure 7(b) exhibits evolution of Fermi surfaces through the $\sqrt{3} \times \sqrt{3}$-to-$\sqrt{21} \times \sqrt{21}$ transition by additional Ag adsorption. As shown in figure 5(c), the $\sqrt{3} \times \sqrt{3}$-Ag surface has an isotropic free-electron-like metallic band. Therefore, the Fermi surface is a complete circle, figure 7(b), and the radius, the Fermi wavevector (k_F), is ~0.1 Å^{-1}. By 0.07 ML-Ag deposition on top of the $\sqrt{3} \times \sqrt{3}$-Ag, k_F of the Fermi surface (the Fermi circle) becomes larger. This indicates electron doping from the Ag adatoms to the $\sqrt{3} \times \sqrt{3}$ surface-state band. When the adatom coverage reaches ~0.14 ML, the $\sqrt{21} \times \sqrt{21}$ phase is formed and much larger Fermi circles are identified over the whole surface Brillouin zones. Despite the non-rigid band shift of

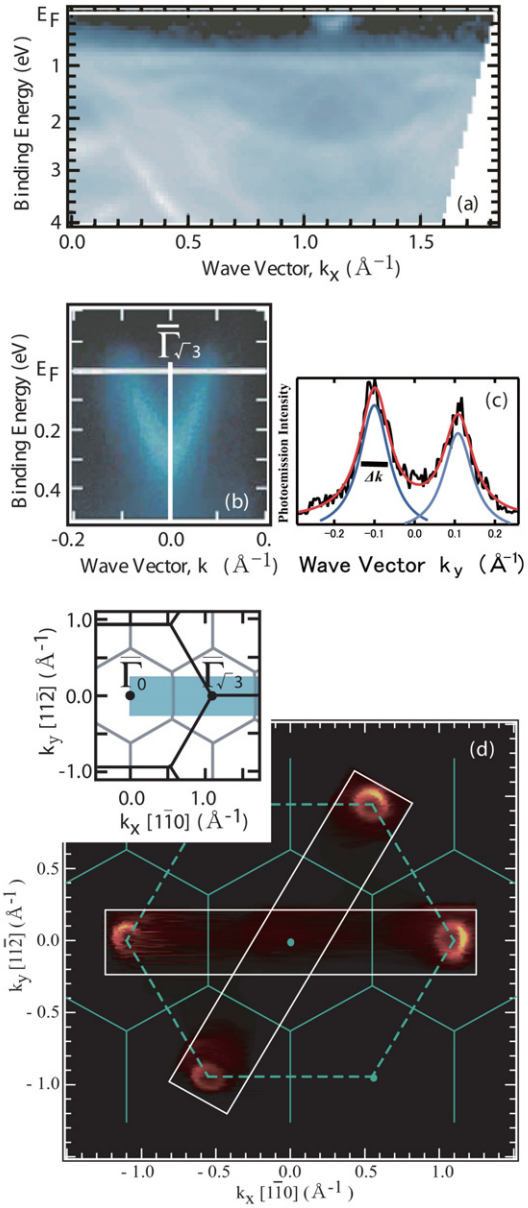

Figure 5. ARPES data of Si(111)$\sqrt{3} \times \sqrt{3}$-Ag surface superstructure. (a) A grey-scale band dispersion image along the [$\bar{1}$10] axis. (b) The magnified grey-scale band dispersion around the centre of the second $\sqrt{3} \times \sqrt{3}$ SBZ ($\bar{\Gamma}_{\sqrt{3}}$). (c) Profile of (b) at E_F, showing the finite width of surface-state peaks, giving an uncertainty in Fermi wavenumber. (d) Fermi surface map [48]. At the centre Brillouin zone ($\bar{\Gamma}_0$), the Fermi ring is missing while it is clearly observed in the second SBZs. The dotted lines show the 1 × 1-SBZ and the solid lines are the $\sqrt{3} \times \sqrt{3}$-SBZ. The inset shows the $\sqrt{3} \times \sqrt{3}$-SBZ. The shaded area is the measured region in (a) and figure 7.

the $\sqrt{3} \times \sqrt{3}$-Ag surface-state band, as described above, the Fermi circle shows free-electron-like behaviour since the hybridization mentioned in figures 6(c)–(e) occurs at energy regions well below the Fermi level.

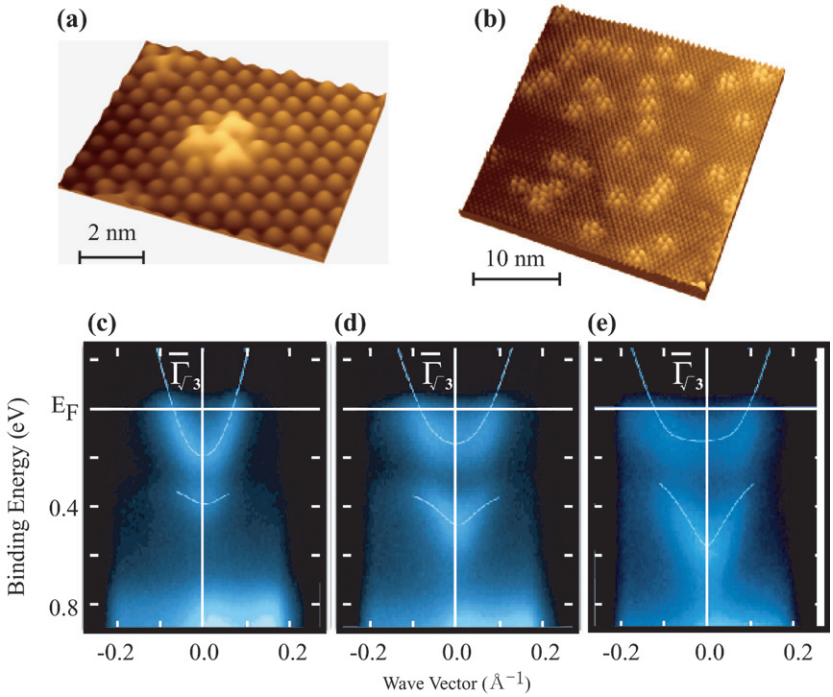

Figure 6. (a) An STM image of a Ag adatom (upper left) and a Ag nanocluster (centre), composed of three Ag adatoms, on the $\sqrt{3} \times \sqrt{3}$-Ag surface taken at 65 K. (b) A wide-area STM image of the $\sqrt{3} \times \sqrt{3}$-Ag covered with Au nanoclusters of 0.02 ML coverage observed at 65 K. (c)–(e) A series of grey-scale band dispersions near $\bar{\Gamma}_{\sqrt{3}}$ of the $\sqrt{3} \times \sqrt{3}$-Ag with Au deposition of (c) 0.01, (d) 0.02, and (e) 0.03 ML, respectively [50]. The measurement was performed at 135 K.

To understand the nature of the photoemission Fermi surface map, we recall the STM image of the $\sqrt{21} \times \sqrt{21}$-Ag surface in figure 8(a). The surface consists of two domains due to rotation of $\pm 10.89°$ with each other. Figure 8(a) shows unit cells of the two domains and the domain boundary across the figure [53]. The photoemission Fermi surface of the $\sqrt{21} \times \sqrt{21}$ surface is then compared with the two $\sqrt{21} \times \sqrt{21}$ surface Brillouin zones (SBZs) as figure 8(b). It is clear that the Fermi circles follow the $\sqrt{21} \times \sqrt{21}$ periodicity in the k space. The same results are also measured for the Si(111)$\sqrt{21} \times \sqrt{21}$-(Ag, Au) as shown in figures 8(c) and (d). In figure 8(f), the Fermi circle of the $\sqrt{21} \times \sqrt{21}$ surface is drawn in an extended SBZ. A schematic drawing of the Fermi surface of the $\sqrt{3} \times \sqrt{3}$-Ag surface is presented in figure 8(e) for a comparison. An area ratio between the Fermi circle and the $\sqrt{21} \times \sqrt{21}$ SBZ indicates three electrons in the $\sqrt{21} \times \sqrt{21}$ unit cell. Because of the 2D electronic system, the electron density n_{2D} can be related to k_F by

$$k_F = \sqrt{2\pi n_{2D}}. \tag{3}$$

Then, n_{2D} can be calculated from the k_F values, 0.16, 0.64, and 1.1×10^{14} cm^{-2} for the pristine $\sqrt{3} \times \sqrt{3}$, the 0.07 ML-Ag added surface, and the $\sqrt{21} \times \sqrt{21}$-Ag, respectively. One can find that the increase in electron density is nearly proportional to the additional Ag coverage because 1 ML $= 7.8 \times 10^{14}$ cm^{-2}. Since the coverage of 0.14 ML corresponds to three adatoms in the $\sqrt{21} \times \sqrt{21}$ unit cell, the adatom is probably ionized as a cation (+1 charge).

Since the Fermi circle is larger than the first SBZ, the first SBZ is fully filled with two electrons. The Fermi circle covers up to the third SBZ and the segments of the Fermi circle in

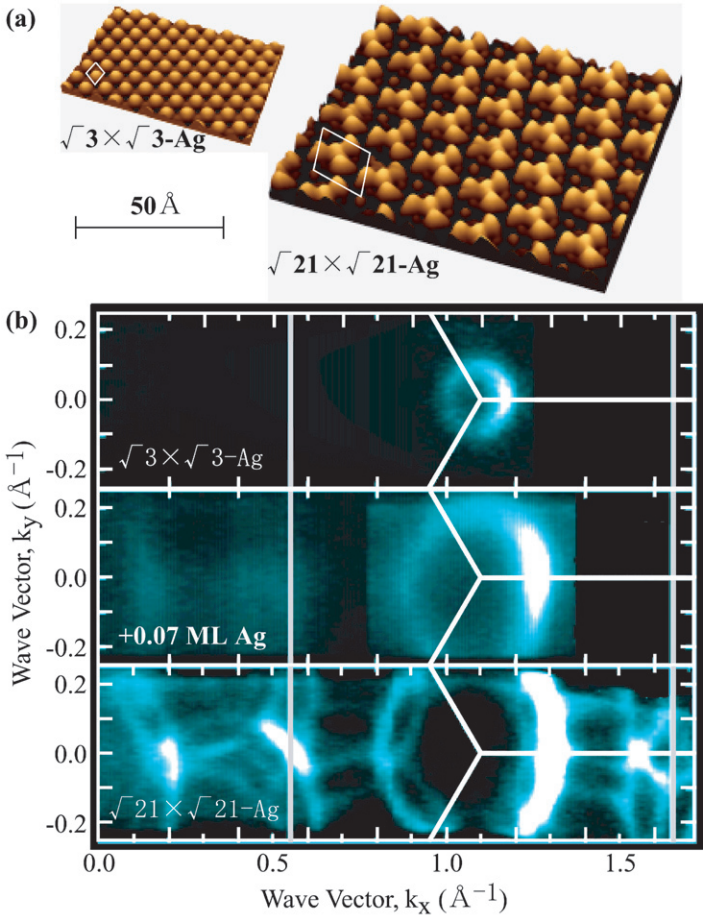

Figure 7. (a) STM images of Si(111)$\sqrt{3} \times \sqrt{3}$-Ag and Si(111)$\sqrt{21} \times \sqrt{21}$-Ag. (b) Evolutions of the Fermi rings by Ag deposition on the $\sqrt{3} \times \sqrt{3}$-Ag at ∼120 K. The additional Ag coverage is 0 ML (the pristine $\sqrt{3} \times \sqrt{3}$-Ag), 0.07 ML, and 0.15 ML (the $\sqrt{21} \times \sqrt{21}$-Ag), respectively. The SBZs of 1×1 and $\sqrt{3} \times \sqrt{3}$ are drawn as grey and white lines, respectively.

the second and third SBZs are depicted in figures 8(g) and (h), respectively. The Fermi ring of the second SBZ consists of a hole pocket centred at the $\bar{\Gamma}_{\sqrt{21}}$ point, while that of the third SBZ is composed of small electron pockets at the $\bar{K}_{\sqrt{21}}$ points.

To study dispersions of the surface-state bands responsible for the Fermi circles, ARPES measurements were performed near E_F. Figure 9 shows experimental energy-versus-wavevector diagrams along a line α–β in figure 8(b). Between E_F and the binding energy $E_B = 0.8$ eV, sharply dispersing parabolic bands are identified. A curve fit to the experimental dispersion indicates that m^* is about 0.29 m_0. The value is almost the same as reported previously for noble-metal-induced $\sqrt{21} \times \sqrt{21}$ phases [42, 53, 55]. In the figure, one can also find that the bands show an energy gap at zone boundaries (ZBs) of the $\sqrt{21} \times \sqrt{21}$ SBZ. For example, along the α–β line (see figure 8(b)), at the ZB of 'relative wavevector' 0.087 Å^{-1}, one can obviously find that the free-electron band energetically splits into two bands, higher (S_{high}) and lower (S_{low}) bands with energy separation (ΔE) of 0.1–0.2 eV at $E_B = 0.3$ eV. This energy splitting at the zone boundary is consistent with a picture of

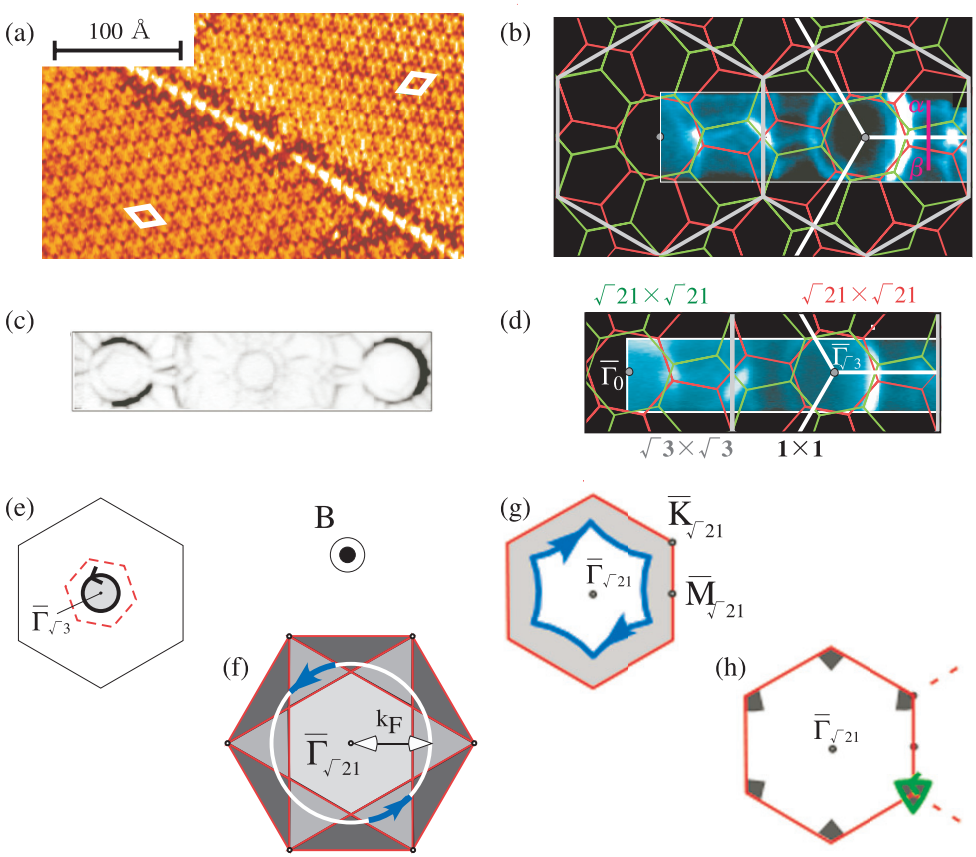

Figure 8. (a) A STM image of two orientational domains of Si(111)$\sqrt{21} \times \sqrt{21}$-Ag separated by a linear boundary. (b) SBZs of the two orientational domains of $\sqrt{21} \times \sqrt{21}$ overlapped on the experimental result of figure 7(b). SBZs of 1×1 and $\sqrt{3} \times \sqrt{3}$ are also shown. The α–β line in (b) is a scanning axis of ARPES measurement shown in figure 9. (c) Photoemission Fermi surfaces of Si(111)$\sqrt{21} \times \sqrt{21}$-(Ag, Au), Crain *et al* [42] (with permission from F J Himpsel). (d) Our result of Fermi surface mapping, overlapped with $\sqrt{21} \times \sqrt{21}\mathrm{R} + 10.98°$ (red, thin), $\sqrt{21} \times \sqrt{21}\mathrm{R} - 10.98°$ (green, thin), $\sqrt{3} \times \sqrt{3}$ (white, thick), and 1×1 (grey, thick) SBZs. (e) Schematic drawing of a Fermi surface of Si(111)$\sqrt{3} \times \sqrt{3}$-Ag in the $\sqrt{3} \times \sqrt{3}$ SBZ. A $\sqrt{21} \times \sqrt{21}$ SBZ is depicted in (e) with dotted lines for a comparison. (f) Superposition of a free-electron Fermi ring for valence 3 on an extended Brillouin zone of $\sqrt{21} \times \sqrt{21}$. (g) The Fermi rings in the reduced second $\sqrt{21} \times \sqrt{21}$ SBZ. (h) The Fermi rings in the reduced third $\sqrt{21} \times \sqrt{21}$ SBZ. The shaded areas correspond to electron-filled regions. Arrows on the peripheries of Fermi surfaces in (e)–(h) show motion of the Fermi electrons under a magnetic field (B) out of the paper [41].

the band folding and the multiple circles with the $\sqrt{21} \times \sqrt{21}$ periodicity in figures 7(b) and 8(c) [42, 55].

To visualize change of the electronic structure through the $\sqrt{3} \times \sqrt{3}$-to-$\sqrt{21} \times \sqrt{21}$ transition, we have performed band calculation based on the nearly-free-electron (NFE) model [2] with the band parameters, m^*, k_F, and ΔE, derived from the present ARPES results. Figure 10 shows an illustration of calculated dispersion curves for Si(111)$\sqrt{3} \times \sqrt{3}$-Ag and Si(111)$\sqrt{21} \times \sqrt{21}$-Ag. In the calculation, seven free-electron bands of one first SBZ and six second SBZs are adopted. Within wavevector regions of $k_x = 0$–0.25 Å^{-1} and

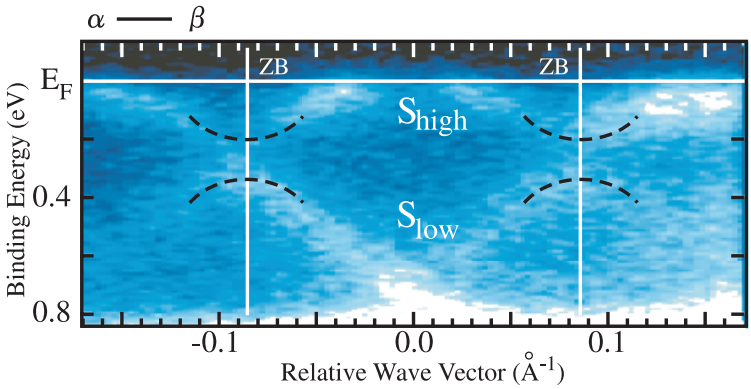

Figure 9. A photoemission band dispersion for the Si(111)$\sqrt{21} \times \sqrt{21}$-Ag surface. The data sets have been compiled from photoemission spectra by mapping angle scans along the α–β line indicated in figure 8(b). The zone boundaries (ZBs) of the $\sqrt{21} \times \sqrt{21}$ SBZ are indicated.

$k_y = 0$–0.25 Å^{-1}, a metallic band of the $\sqrt{3} \times \sqrt{3}$-Ag is free-electron-like. On the other hand, in this k-region, Si(111)$\sqrt{21} \times \sqrt{21}$-Ag has symmetry points, $\bar{K}_{\sqrt{21}}$ and $\bar{M}_{\sqrt{21}}$, and a ZB. Through the band-folding effect, there exist three bands below E_F and the energy gap at $\sqrt{21} \times \sqrt{21}$ ZBs. The values of the energy gaps at $\sqrt{21} \times \sqrt{21}$ ZBs are reproduced by setting the Fourier coefficient of potential energy, U, to -75 meV. The overall band structure based on the NFE model agrees well with the photoemission results described above. It is noted that bands in the second and third SBZs are degenerate at the $\bar{K}_{\sqrt{21}}$ point. In contrast, NFE calculation with positive U value results in degeneracy of bands in the first and second SBZs, which is different from the experimental results. Since the positive and negative values of U imply repulsive and attractive potentials, respectively, surface state electrons of the $\sqrt{21} \times \sqrt{21}$ phase feel the attractive potential of the $\sqrt{21} \times \sqrt{21}$ period. This seems consistent with a picture that the adatoms are ionized as cations on the surface, as mentioned above.

2.2. Electrical conduction through surface atomic layers

Among many surface superstructures on Si(111), the $\sqrt{21} \times \sqrt{21}$ phase has attracted considerable interest in surface transport phenomena [16]. Deposition of any noble-metal atoms of less than a monolayer on the $\sqrt{3} \times \sqrt{3}$-Ag surface increases the conductivity significantly. The maximum conductivity is obtained at the $\sqrt{21} \times \sqrt{21}$ formation with around 0.14 ML coverage of noble metals, indicating a close relation between the high electrical conductivity and the superstructure formation [52]. The transport experiments have been performed with the FPP method with macroscopic probe spacing [16].

In general, the conductivity is originated from three electrical channels, surface-state bands of the topmost atomic layers, bulk-state bands in the surface space-charge layer beneath the surface, and bulk-state bands in the inner crystal [16]. Since the measurements have been performed *in situ* in UHV using the same Si wafer with different surface superstructures, the transport change is only described with the first two channels. As described below, there exist excess holes in the surface space-charge layer beneath the $\sqrt{3} \times \sqrt{3}$-Ag phase, which are depleted when the surface transforms to the $\sqrt{21} \times \sqrt{21}$ phase [45]. Therefore, the conductivity in the surface space-charge layer should decrease through the $\sqrt{3} \times \sqrt{3}$-to-$\sqrt{21} \times \sqrt{21}$ transition, which is opposite to the experimental fact. Therefore, the surface-state channel is responsible for the increase of electrical conductivity. The research has demonstrated, for the

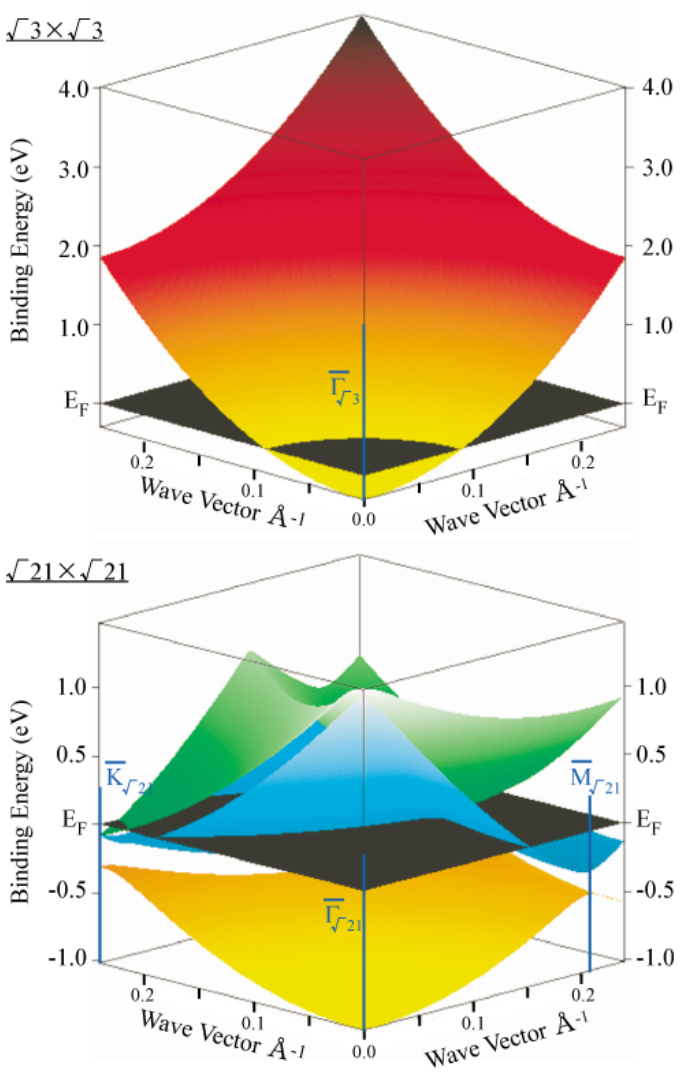

Figure 10. Empirical band calculation of Si(111)$\sqrt{3} \times \sqrt{3}$-Ag (upper) and Si(111)$\sqrt{21} \times \sqrt{21}$-Ag (lower). The calculation is based on the nearly-free-electron (NFE) model with band parameters determined by photoemission spectroscopy. The position of the Fermi level is depicted as a black sheet. Intersections of the sheet and the bands trace the shape of the Fermi surface.

first time, measurement of electronic transport through a surface atomic layer, not through the bulk states [16].

Recently, we have developed a new experimental set-up to measure both longitudinal resistance and transverse resistance (Hall resistance) of a surface simultaneously with magnetic field applied perpendicular to the surface [41], as schematically drawn in figure 11. The four tungsten (W) wires (0.3 mm in diameter) for voltage probes were pressed on the sample surface before installation into the UHV chamber. The current flows between the two tantalum (Ta) clamps at the sample ends. The longitudinal voltage (V_{xx}) and Hall voltage (V_{H}) are measured simultaneously as functions of the current and magnetic field. The previous surface

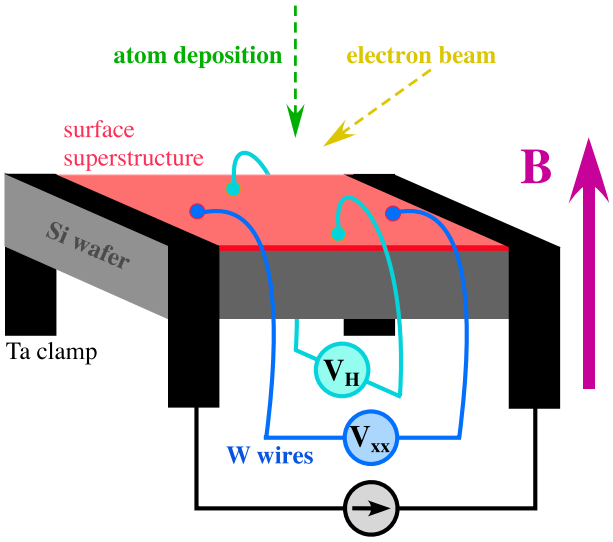

Figure 11. A schematic drawing of the experimental set-up for the galvanomagnetic transport measurement with a silicon wafer. Magnetic field (B) is applied normal to the surface. A pair of tantalum (Ta) clamps is for the current source and two pairs of tungsten (W) wire-contact electrodes are for voltage probes. The probe spacings were 9.6 and 3 mm for the longitudinal (V_{xx}) and Hall ($V_{\rm H}$) voltage measurements, respectively. The electron beam is irradiated on a sample surface to observe reflection high energy electron diffraction patterns. Deposition is possible during the conductivity measurement.

conductivity experiments [52] correspond to measurements of V_{xx} only, without magnetic field. The macroscopic probe spacing in the millimetre range enables conductivity measurement during metal deposition and reflection high energy electron diffraction observation to confirm the surface superstructure, while the sensitivity to the surface is low. The magnetic field of ± 6 T is applied with a superconducting coil.

We now describe how to obtain the surface-state electrical conductivity of the surface superstructures from the present experimental set-up with macroscopic probe spacing, and then compare the results quantitatively with the values estimated from the photoemission Fermi surfaces and band dispersion. Figure 12(a) shows the change in electrical conductivity of a Si(111) wafer, deduced from the longitudinal voltage (V_{xx}), during the Au deposition on the $\sqrt{3} \times \sqrt{3}$-Ag surface at RT. The conductivity increases steeply from the beginning and reaches the maximum at Au coverage $\Theta = 0.14$ ML where the $\sqrt{21} \times \sqrt{21}$ superstructure is formed. In the inset of figure 12(a), the measured electrical resistance, R_{xx}, is also shown. The longitudinal resistance R_{xx} is converted to the change of sheet conductivity $\Delta\sigma$ through a relation [16],

$$\Delta\sigma = \frac{L}{W}\left(\frac{1}{R_{xx}} - \frac{1}{R_0}\right), \tag{4}$$

where L and W are the length (9.6 mm) and width (4.0 mm) of the measured surface area, and R_0 is the longitudinal resistance before the Au deposition.

As described above, the measured conductivity consists of three electrical channels, the topmost surface-state atomic layer (ss), space-charge layers (sc), and inner bulk layers (b). In two-dimensional systems, this is given by [16]

$$\sigma = \sigma_{\rm ss} + \sigma_{\rm sc} + \sigma_{\rm b} d, \tag{5}$$

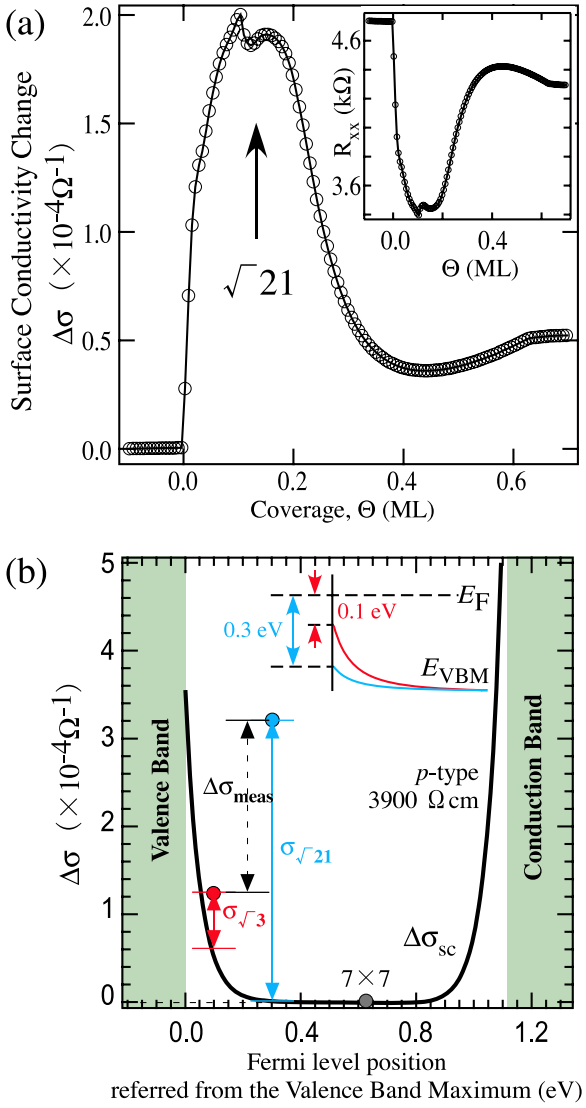

Figure 12. (a) Change in electrical conductivity during Au deposition on the Si(111)$\sqrt{3} \times \sqrt{3}$-Ag surface at RT. Coverage dependence of the longitudinal resistance, R_{xx}, is shown in the inset. (b) Summary of conductivity changes ($\Delta\sigma$). A solid curve shows the excess electrical conductivity through the surface space-charge layer, $\Delta\sigma_{sc}$, calculated as a function of surface E_F position for a Si wafer of p type (3900 Ωcm resistivity). Data points indicate the measured values of excess conductivity ($\Delta\sigma_{meas}$), $\sqrt{3}\times\sqrt{3}$-Ag ($\Delta\sigma_{\sqrt{3}}$) and $\sqrt{21}\times\sqrt{21}$-(Ag, Au) ($\Delta\sigma_{\sqrt{21}}$) with respect to that of the 7×7 clean phase. It is noted that $\Delta\sigma_{meas}$ corresponds to the maximum conductivity change in (a). The points are plotted at surface E_F position determined by previous photoemission reports. Band bending of the $\sqrt{3} \times \sqrt{3}$ ($E_F - E_{VBM} = 0.1$ eV, red) and $\sqrt{21} \times \sqrt{21}$ ($E_F - E_{VBM} = 0.3$ eV, blue) phases is schematically depicted in the inset.

where d is the wafer thickness. In the present experimental set-up (figure 11), the bulk contribution dominates the measured resistance because of the poor surface sensitivity due to the macroscopic probe spacing. But the bulk contribution is kept constant during the surface transformation. Therefore, the measured change in conductivity (figure 12(a)) originates only

from the surface-state and the space-charge layers:

$$\Delta\sigma = \Delta\sigma_{ss} + \Delta\sigma_{sc}. \tag{6}$$

On one hand, σ_{sc} and $\Delta\sigma_{sc}$ can be calculated by the Poisson equation once one knows the band bending beneath the surface. The amount of band-bending under the surface can be measured by, for example, core-level photoemission spectroscopy [16, 45]. The amount of band-bending is expressed in terms of the difference in Fermi-level position between that at the surface and in the bulk. Excess carriers are accumulated, or carriers are depleted due to the band bending. Figure 12(b) exhibits the excess electrical conductivity, $\Delta\sigma_{sc}$, through the space-charge layer as a function of the surface E_F position. The carrier mobility was assumed to be the same as the bulk value. The electrical conductivity under the flat-band condition, where the surface E_F and bulk E_F are equal, is defined as the reference ($\Delta\sigma = 0$). The measured conductivities of the $\sqrt{3}\times\sqrt{3}$-Ag and $\sqrt{21}\times\sqrt{21}$-(Ag, Au) are also plotted at their surface E_F positions. The Si(111)7×7 clean surface has its surface E_F position almost at the centre of the Si bulk band gap (0.63 eV above the valence-band maximum) and therefore the space-charge layer is depletion type. The conductivity of the 7×7 surface state is several orders of magnitude lower than that of the space-charge layer [56]. Therefore, the conductivity of the 7×7 surface is a good experimental reference because it almost corresponds to the electrical conductivity under the flat-band condition with negligible surface-state conductivity [16]. From the previous photoemission spectroscopy, the surface E_F positions of the $\sqrt{3}\times\sqrt{3}$-Ag and $\sqrt{21}\times\sqrt{21}$-(Ag, Au) phases are ~0.1 and ~0.3 eV, respectively, above the valence-band maximum [45]. Then, the σ_{ss} values of these phases are given by subtracting the calculated space-charge-layer conductivity from the measured total conductivities, as shown in figure 12(b). The surface-state conductivity of the $\sqrt{3}\times\sqrt{3}$-Ag is $\sim0.7\times10^{-4}\ \Omega^{-1}\ \square^{-1}$ and that of the $\sqrt{21}\times\sqrt{21}$-(Ag, Au) is $\sim3.2\times10^{-4}\ \Omega^{-1}\ \square^{-1}$.

As shown in figure 5(d), the $\sqrt{3}\times\sqrt{3}$-Ag phase possesses an isotropic circular Fermi surface. As shown in figures 7 and 8, on the other hand, the $\sqrt{21}\times\sqrt{21}$ phase shows complicated spectral features of the Fermi surface due to contribution of two orientational domains, extending over the second and third SBZs [29, 42]. Since equation (1) implies that the integral should be performed on the Fermi surface in the reduced zone scheme, contributions from all segments of Fermi surface in all reduced zones should be summed up. As shown in figure 8, a summation of all the portions of the $\sqrt{21}\times\sqrt{21}$ Fermi circles in the second and third SBZs produces a single Fermi circle in the extended zone scheme. Furthermore, the gap formation at the zone boundaries (figure 9) is so small that it hardly perturbs the energy dispersion at E_F. Therefore, the $\sqrt{21}\times\sqrt{21}$ electronic structure is also reasonably regarded as an isotropic free-electron system.

Since both of the $\sqrt{3}\times\sqrt{3}$-Ag to $\sqrt{21}\times\sqrt{21}$ phases are represented by a nearly 2D free-electron model, the density of states at E_F is written as $\mathcal{D} = m^*/(\pi\hbar^2)$, which can be calculated by using the value of m^* obtained from the band dispersion. The Fermi velocity is given by $v_F = \hbar k_F/m^*$, which can be calculated by using the value of Fermi wavenumber k_F obtained from the photoemission result. Thus, from the band parameters determined by ARPES, m^* and k_F of the two surface phases, $\mathcal{D}^{2D}$ and v_F are estimated as in table 1. $\mathcal{D}$ and v_F of the $\sqrt{21}\times\sqrt{21}$ phase are 92% and 35% larger than those of $\sqrt{3}\times\sqrt{3}$, respectively. From the peak width of the surface state at E_F as shown in figure 5(c), the uncertainty of Fermi wavenumber Δk_F is obtained. This value is related to the carrier mean free path ℓ according to the uncertainty principle, $\ell\Delta k_F \sim 1$. So the mean free path is calculated as shown in table 1. Then the carrier relation time τ is calculated by $\tau = \ell/v_F$. Thus we can obtain all quantities necessary for the calculation in equation (2). As a consequence, if the Boltzmann picture is assumed, the conductivity σ_{PES} is calculated only

Table 1. Various parameters of the metallic surface states of Si(111)$\sqrt{3}\times\sqrt{3}$-Ag and $\sqrt{21}\times\sqrt{21}$-Ag superstructures, determined by photoemission spectroscopy. The surface-state conductivity $\sigma_{\rm PES}$ is calculated from equation (2) using these parameters. The last row shows the values of surface-state conductivity $\sigma_{\rm FPP}$ measured by the FPP method directly.

Physical quantity	Unit	$\sqrt{3}\times\sqrt{3}$-Ag	$\sqrt{21}\times\sqrt{21}$-Ag
Fermi wavenumber, $k_{\rm F}$	(Å^{-1})	0.10[a]	0.26
Its uncertainty[a], $\Delta k_{\rm F}$	(Å^{-1})	∼0.061[a]	∼0.036
Effective mass, m^*	$m_{\rm e}$	0.13[a]	0.25
Electron density, $n(=k_{\rm F}^2/2\pi)$	(10^{14} cm^{-2})	0.16	1.1
Density of states, $\mathcal{D}(=m^*/\pi\hbar^2)$	(10^{13} eV^{-1} cm^{-2})	5.4	10
Fermi velocity, $v_{\rm F}(=\hbar k_{\rm F}/m^*)$	(10^{8} cm s^{-1})	0.89	1.2
Mean free path, $l(=1/\Delta k)$	(Å)	∼17	∼28
Carrier relaxation time, $\tau(=l/v_{\rm F})$	(10^{-15} s)	∼1.9	∼2.4
Conductivity (PES)[b], $\sigma_{\rm PES}$	(10^{-4} Ω^{-1})	∼0.65	∼2.7
Conductivity (FPP)[b], $\sigma_{\rm FPP}$	(10^{-4} Ω^{-1})	∼0.75	∼3.2

[a] Reference [47].
[b] References [16, 57].

from the photoemission data, as shown in table 1. The conductivity increases by 2×10^{-4} Ω^{-1} through the $\sqrt{3}\times\sqrt{3}$-to-$\sqrt{21}\times\sqrt{21}$ transition. The value of $\Delta\sigma$ is consistent with the result in figure 12(a).

On the other hand, the surface-state conductivity of these surfaces was separately measured by the FPP method, which is listed by $\sigma_{\rm FPP}$ in table 1 [16, 57]. The values are reasonably consistent with $\sigma_{\rm PES}$ within the experimental errors. This means that the Boltzmann picture works for the surface-state electrical conduction of the $\sqrt{3}\times\sqrt{3}$-Ag and $\sqrt{21}\times\sqrt{21}$ surfaces. The mean free path ℓ at room temperature is around 20 Å, which is one order of magnitude smaller than those in bulk Ag metal [2]. According to STM observations, the distances between steps, domain boundaries, and point defects are of the order of 1000 Å, which is much larger than ℓ. Therefore, carrier scattering in the surface states is dominated by phonons, not by the static defects.

2.3. Hall effect in surface atomic layers

When magnetic field (B) is applied perpendicular to these surfaces, electrons move along the Fermi surfaces in reciprocal space [2]. The electrons in the $\sqrt{3}\times\sqrt{3}$-Ag phase take a counterclockwise orbit (an electron-like orbit) as shown in figure 8(e). Electron motion in the $\sqrt{21}\times\sqrt{21}$-(Ag, Au) phase is also depicted as a counterclockwise orbit in the extended zone scheme (figure 8(f)). However, since the Fermi surface is larger than the surface Brillouin zone (SBZ), the actual feature must be described in the reduced zone scheme. As shown in figures 8(g) and (h), due to the back-folding of the Fermi surface and band, the electrons of $\sqrt{21}\times\sqrt{21}$-(Ag, Au) take a large clockwise orbit (a hole-like orbit) in the second SBZ and a small counterclockwise orbit (an electron-like orbit) in the third SBZ. Therefore, the major Fermi electrons of $\sqrt{21}\times\sqrt{21}$-(Ag, Au) show hole-like behaviour, while those of $\sqrt{3}\times\sqrt{3}$-Ag are electron-like. Since the majority carriers in the surface states are thus expected to be changed, the Hall effect measurement is necessary to confirm it [41].

Since the Hall coefficient, $R_{\rm H}$, is expressed as for the high field limit

$$R_{\rm H}=-\frac{1}{e(N_{\rm n}-N_{\rm p})}, \tag{7}$$

and for the low field limit

$$R_{\mathrm{H}} = -\frac{N_{\mathrm{n}} - N_{\mathrm{p}}}{e(N_{\mathrm{n}} + N_{\mathrm{p}})^2}, \tag{8}$$

where $N_{\mathrm{n(p)}}$ is the number of carriers with electron(hole)-like behaviour, according to the consideration described above, R_{H} should be negative for the $\sqrt{3} \times \sqrt{3}$-Ag and positive for the $\sqrt{21} \times \sqrt{21}$-(Ag, Au) if we consider the surface state only. On the other hand, the surface space-charge layers beneath these superstructures are inversion (accumulation) and depletion layers for the $\sqrt{3} \times \sqrt{3}$-Ag and $\sqrt{21} \times \sqrt{21}$-(Ag, Au) phases, respectively, on an $n(p)$-type Si wafer. As a consequence, through the $\sqrt{3} \times \sqrt{3}$-to-$\sqrt{21} \times \sqrt{21}$ transition, N_{p} should decrease and R_{H} should be positive and become larger in the surface space-charge layer. This occurs irrespective of whether the substrate Si crystal is n type or p type. However, this change is opposite to that expected in the surface state; N_{p} increases and R_{H} changes from negative to positive according to the consideration in figures 8(e)–(h). Therefore, entirely opposite changes of the Hall coefficient are expected, which also leads to direct distinction between the contributions from the surface state and from the space-charge layer. However, as described below, the experiments show that the R_{H} does not change in sign, remaining positive through the transition. This is due to the parallel detection of the contributions from the surface space-charge layer and from the surface state. But the results clearly show the contribution from the surface state in the Hall effect, as clarified below.

The Hall resistance, R_{Hall} ($=R_{\mathrm{H}}B = V_{\mathrm{H}}/I$), measured with the Hall voltage probes in figure 11, has increased linearly with magnetic field as shown in figure 13(a). The gradients, R_{H}, obtained by line-fit to experimental curves are positive, and the value is smaller for $\sqrt{21} \times \sqrt{21}$-(Ag, Au) than for $\sqrt{3} \times \sqrt{3}$-Ag. From the definition of R_{H}, this clearly indicates an increase in carrier density behaving as holes by the $\sqrt{3} \times \sqrt{3}$-to-$\sqrt{21} \times \sqrt{21}$ transition. This is an unambiguous detection of the Hall effect of carriers in the surface state because, as mentioned above, an opposite change in R_{H} is expected from the surface space-charge layer.

In the inset of figure 13(a), the change in longitudinal resistance $\delta R_{xx}(= R_{xx}(B) - R_{xx}(B = 0))$ (magnetoresistance) shows nearly parabolic dependence on the magnetic field. Since the value of $\omega_{\mathrm{c}}\tau = \frac{eB}{m^*}$ of the surface state reaches ∼0.05 at most in the present experimental apparatus, the measurement has been performed in the low field limit ($\omega_{\mathrm{c}}\tau \ll 1$), and R_{xx} can be fitted by [58]

$$\frac{R_{xx}(B) - R_{xx}(B = 0)}{R_{xx}(B = 0)} = \xi \mu_{\mathrm{H}}^2 B^2, \tag{9}$$

where μ_{H} is the Hall mobility of carriers and ξ is a constant governed by the scattering mechanism of carriers ($\xi \sim 0.273$ for acoustic phonon scattering, which is dominant at room temperature). The μ_{H} values determined by the parabolic curve-fits are 430 and 440 cm^2 V s^{-1} for the $\sqrt{3} \times \sqrt{3}$-Ag and $\sqrt{21} \times \sqrt{21}$-(Ag, Au) surfaces, respectively. These values are close to the hole mobility in the bulk Si crystal ($\mu_{\mathrm{H}} = 480$ cm^2 V s^{-1}) [28, 59]. This means that the present data measured by the macroscopic FPP method contain the conductivity of the surface to a certain degree, although those of the bulk and space-charge layer are dominant. Therefore, to extract the surface-state Hall effect, we need more quantitative discussion by focusing on differences in R_{xx} and R_{Hall} between the two surface structures.

Decomposition of the experimental results of conductivities and Hall coefficients into the contributions from the surface state and surface space-charge layer is done by adopting the two-layer model [58]. In the model, it is essential to introduce a quantity, $R_{\mathrm{H}}\sigma^2$, and the measured *change* of this quantity is a sum of those from the surface state and space-charge layer:

$$\Delta(R_{\mathrm{Hmea}}\sigma_{\mathrm{mea}}^2) = \Delta(R_{\mathrm{Hss}}\sigma_{\mathrm{ss}}^2) + \Delta(R_{\mathrm{Hsc}}\sigma_{\mathrm{sc}}^2). \tag{10}$$

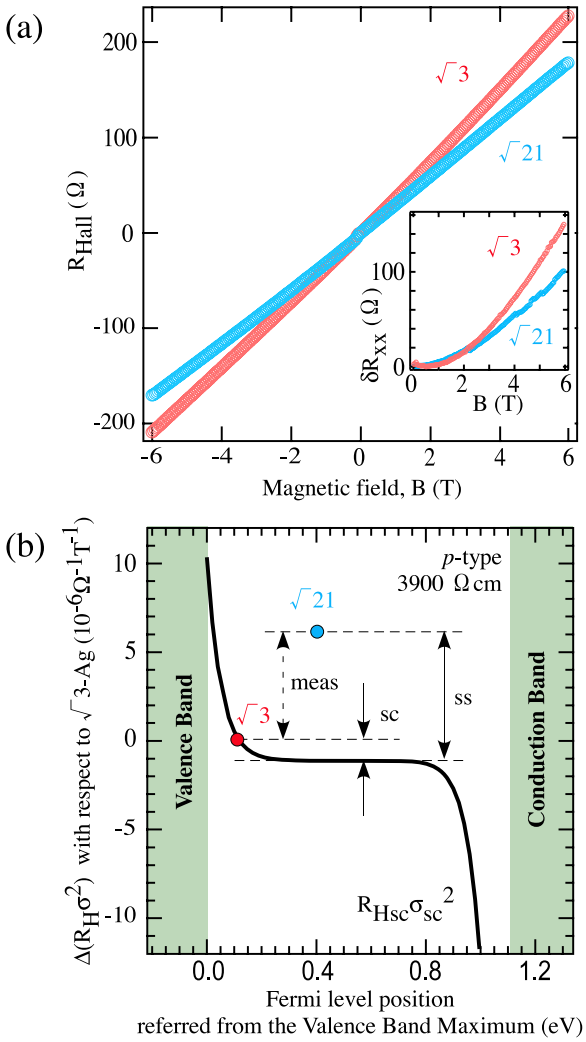

Figure 13. (a) Hall resistance of the $\sqrt{3} \times \sqrt{3}$-Ag (red) and $\sqrt{21} \times \sqrt{21}$-(Ag, Au) surface superstructures (blue) [41]. The inset shows changes in the longitudinal resistance with magnetic field. (b) The value of $\Delta(R_H\sigma^2)$ plotted as a function of the surface Fermi level position with respect to the Si bulk valence-band maximum for a p-type (3900 Ω cm) Si wafer. The calculated results are given by solid curves ($R_{Hsc}\sigma_{sc}^2$)) while the experimental values are indicated by circles for Si(111)$\sqrt{3} \times \sqrt{3}$-Ag ($\sqrt{3}$) and Si(111)$\sqrt{21} \times \sqrt{21}$-(Ag, Au) ($\sqrt{21}$). Arrows labelled 'meas' correspond to change in (a) while 'ss (sc)' represents the surface-state (space-charge layer) component.

The components of the space-charge layer can be calculated by solving Poisson's equation [16]. Then the surface state components can be obtained from equation (10).

The solid curve in figure 13(b) shows $R_{Hsc}\sigma_{sc}^2$ values calculated as a function of the Fermi-level position at the surface. The $\Delta(R_{Hsc}\sigma_{sc}^2)$ between the $\sqrt{3}$-Ag and $\sqrt{21}$-(Ag, Au) is $\sim -1.5 \times 10^{-6}\ \Omega^{-1}\ T^{-1}$. As expected previously, this change is the opposite to the measured results, which are plotted in figure 13(b), $\Delta(R_{Hmea}\sigma_{mea}^2) > 0$. Then, from equation (10), $\Delta(R_{Hss}\sigma_{ss}^2)$ is now determined to be $\sim +7.5 \times 10^{-6}\ \Omega^{-1}\ T^{-1}$.

We have estimated the value of $\Delta(R_{\mathrm{Hss}}\sigma_{\mathrm{ss}}^2)$ in another way by using photoemission data only. We have used the σ_{PES} in table 1 as the surface-state conductivity σ_{ss}. The Hall coefficient R_{Hss} is calculated from equation (8) with the carrier densities N_{n} and N_{p}. The carrier density in the $\sqrt{21} \times \sqrt{21}$-(Ag, Au) phase can be calculated from the Fermi surfaces in figures 8(g) and (h); the area fraction of the unoccupied states in the second SBZ gives $N_{\mathrm{p}} = 4.3 \times 10^{13}$ cm^{-2}, and the area fraction of the occupied states in the third SBZ gives $N_{\mathrm{n}} = 0.4 \times 10^{13}$ cm^{-2}. As a result, we obtain $R_{\mathrm{Hss}} = +11\ \Omega\ \mathrm{T}^{-1}$. On the other hand, for the $\sqrt{3} \times \sqrt{3}$-Ag phase, the N_{n} is estimated from the Fermi surface in figure 8(e), $N_{\mathrm{n}} = 1.6 \times 10^{13}$ cm^{-2}, giving $R_{\mathrm{Hss}} = -39\ \Omega\ \mathrm{T}^{-1}$. The surface-state conductivity is also given by σ_{PES} in table 1. Finally we obtain the value of $\Delta(R_{\mathrm{Hss}}\sigma_{\mathrm{ss}}^2) \sim 1.3 \times 10^{-6}\ \Omega^{-1}\ \mathrm{T}^{-1}$, which should be compared with the value calculated from the transport measurements. Both are of the same order though there is a discrepancy in the quantitative value. The discrepancy may come from several reasons, (1) errors in the mobility in the surface space-charge layer used in the calculation of σ_{sc}, (2) overestimate of the carrier density in surface states from photoemission data (some of them may not be mobile due to trapping in defect states), and (3) change in dopant concentration near the surface. But the semi-quantitative agreement between the Hall effect results and photoemission results indicates that the Hall effect in surface states is actually detected.

As shown in this section, the parameters of surface electronic structures determined by photoemission mapping of the Fermi surface and band dispersion are quite consistent with the transport properties directly measured by the FPP methods. This means that the surface system described here is so 'clean' that the Boltzmann picture works well. If the carrier mean free path is so small due to high-density defects, hopping-type conduction should be taken into account instead of the Boltzmann picture [34].

3. Anisotropic quasi-one-dimensional metal

In this section, we briefly introduce a case of quasi-1D metallic surface superstructure, the Si(111)4 × 1-In surface. As shown in figure 14(b), its atomic arrangement is a massive array of metallic quantum wires composed of four lines of In atom chains running along the $[10\bar{1}]$ direction, each wire being separated by a Si-atom chain in between the metallic wires. This surface superstructure is contrasted to the isotropic Si(111)$\sqrt{3} \times \sqrt{3}$-Ag surface described in the previous section. The $\sqrt{3} \times \sqrt{3}$-Ag surface has a circular Fermi surface (isotropic 2D metal), while the 4 × 1-In surface has an almost straight Fermi surface (Fermi lines) as shown in figure 3(a), which is illustrated in figure 2(e). Figure 14(a) shows a schematic drawing of the Fermi lines and experimental dispersion curves of three 1D surface-state bands [22, 60, 61]. The bands show parabolic dispersions around the $\overline{\mathrm{X}}$ point along the $\overline{\Gamma}$–$\overline{\mathrm{X}}$ direction (along the In chain), while they do not show significant dispersion in the perpendicular direction. Because of the quasi-1D electronic structure, therefore, the surface-state transport is expected to be highly anisotropic, with a higher conductivity along the In wires than across the wires.

There is one more interesting thing which is characteristic of the quasi-1D metallic systems. Almost straight lines in the Fermi surface satisfy the nesting condition, which leads to a charge-density-wave (CDW) transition. Actually, the 4 × 1-In surface is known to reveal a phase transition by cooling; the 4 × 1 changes to an 8 × '2' superstructure around 130 K [22]. This periodicity doubling correspond to the nearly half-filled bands m2 and m3 in figure 14(a); the Fermi lines bisect the SBZ. Due to the CDW transition (Peierls transition), the surface becomes insulating, resulting in a drastic decrease in surface conductivity [38].

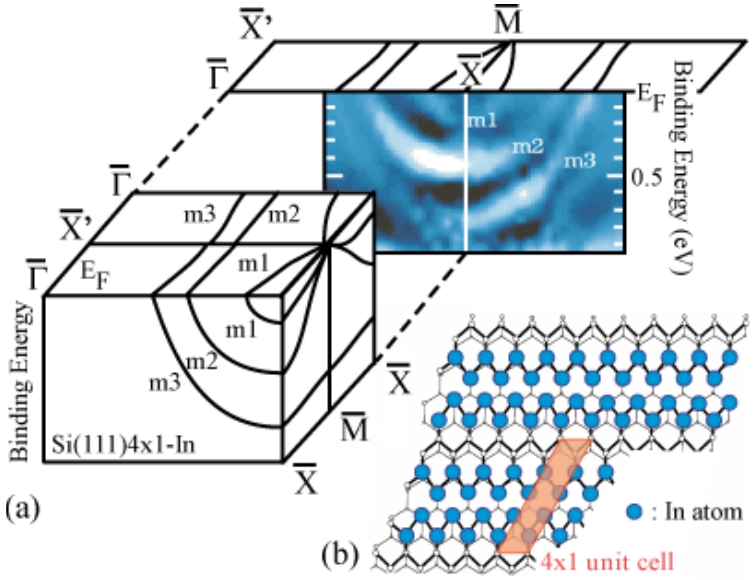

Figure 14. (a) Schematic drawing of Fermi surfaces and band dispersion of 1D metallic surface-state bands (m1, m2, and m3) of Si(111)4 × 1-In, determined by Abukawa *et al* [60] and Yeom *et al* [22]. (b) Structure model of this surface [61].

Before discussing the quasi-1D transport phenomena, we describe the microscopic four-point probe method (MFPP) for measuring surface transport using μm spacing between probes [35]. This method is much more surface sensitive than the macroscopic one described in figure 11, since the measuring current flows mainly near the surface. We have demonstrated that the measured resistance directly corresponds to the surface layer [34, 35, 37–40].

When the MFPP is placed at the centre of a macroscopic sample surface (mm–cm in size), the sample can be regarded as infinitely large, so that the measured resistance can be analytically calculated by solving Poisson's equation [62]: the resistances of an infinitely large 2D layer/sheet measured with linear MFPP (figure 15(a)) and square MFPP (figure 15(c)) arrangements with equidistant probe spacings should be

$$R_{\text{linear}} = \Delta V/I = \frac{1}{\pi\sqrt{\sigma_x\sigma_y}}\ln 2, \tag{11}$$

$$R_{\text{square}} = \Delta V/I = \frac{1}{2\pi\sqrt{\sigma_x\sigma_y}}\ln\left(1+\frac{\sigma_y}{\sigma_x}\right), \tag{12}$$

respectively. ΔV is voltage drops measured by an inner pair of probes in the linear MFPP or by any pair of adjacent probes in the square MFPP. I is the measuring current flowing through another pair of probes. σ_x and σ_y are conductivities along x and y directions, respectively, with the sample surface being on the xy plane. Then one can notice an important fact from equations (11) and (12). Even if the probes are rotated by 90° with respect to the sample surface having anisotropic conductivity, the linear MFPP measurement gives the same value of resistance; σ_x and σ_y are just exchanged with each other in equation (11). This is true for any angles of rotation of the probes in the linear MFPP, meaning that R_{linear} always gives a geometric mean of σ_x and σ_y only. The square MFPP, however, gives different values of resistance by exchanging σ_x and σ_y in equation (12) when the square is rotated by 90° or when another combination of current and voltage probes is selected. Thus, anisotropy in conductivity

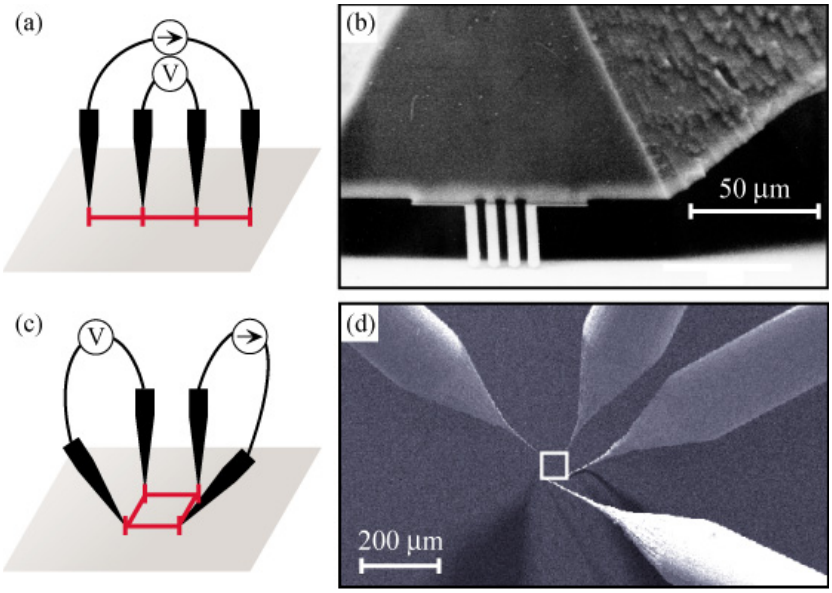

Figure 15. (a) A schematic drawing of the linear FPP method. Current and voltage probes are indicated. (b) A scanning electron microscope (SEM) image of a monolithic MFPP contacting the sample surface during surface conductivity measurements. (c) A schematic drawing of the square FPP method. (d) A SEM image of the four independently driven STM tips during measurements.

of infinite 2D sheets can be measured only by the square MFPP method, and σ_x and σ_y are obtained separately from the two values of resistance measured by two combinations of current and voltage probes.

Figures 15(b) and (d) show scanning electron microscope images of the MFPP methods with monolithic MFPP and four independently driven STM tips, respectively [35]. The former probe is simple to operate and it is easy to extend the measurement with temperature variation. On the other hand, the four-tip STM system is complicated but it allows any arrangement of four probes. In this section, we introduce the measurements with the four-tip STM system [40].

The lower right inset of figure 16(b) shows an STM image of the Si(111)4 × 1 surface, where the In chains run horizontally. Figure 16(a) gives I–V curves measured with the linear MFPP with 60 μm probe spacing aligned parallel and perpendicular to the In chains. The SEM images of the probes are shown in the insets. The outer two probes are current probes while the inner ones are voltage probes. The values of resistance measured in the two directions were essentially the same; the gradients of the I–V curves give almost the same resistances, 4.6 and 5.1 kΩ, within experimental error.

Figure 16(b) shows I–V curves measured by the square MFPP method. ΔV_{ij} is a voltage drop measured between probe i and probe j, with current flowing from probe k to probe l, I_{kl} (see the upper left inset of the SEM image). Two values of resistance, $\Delta V_{23}/I_{14} = 192\ \Omega$ and $\Delta V_{43}/I_{12} = 10.3\ \text{k}\Omega$, were obtained from the gradients of the respective I–V curves, just by changing the combination of current and voltage probes. A line linking probe 1 (2) with probe 4 (3) is parallel to the In chains, while that connecting probe 1 (3) and probe 2 (4) is perpendicular to the chains. The results indicate that an exchange of σ_x ($=\sigma_\perp$, perpendicular to the In chains) and σ_y ($=\sigma_\parallel$, parallel to the In chains) in equation (12) results in ∼60 times difference in the measured resistance. This clearly demonstrates a detection of the anisotropy in conductivity, and also means a direct detection of surface-state conductivity (because the

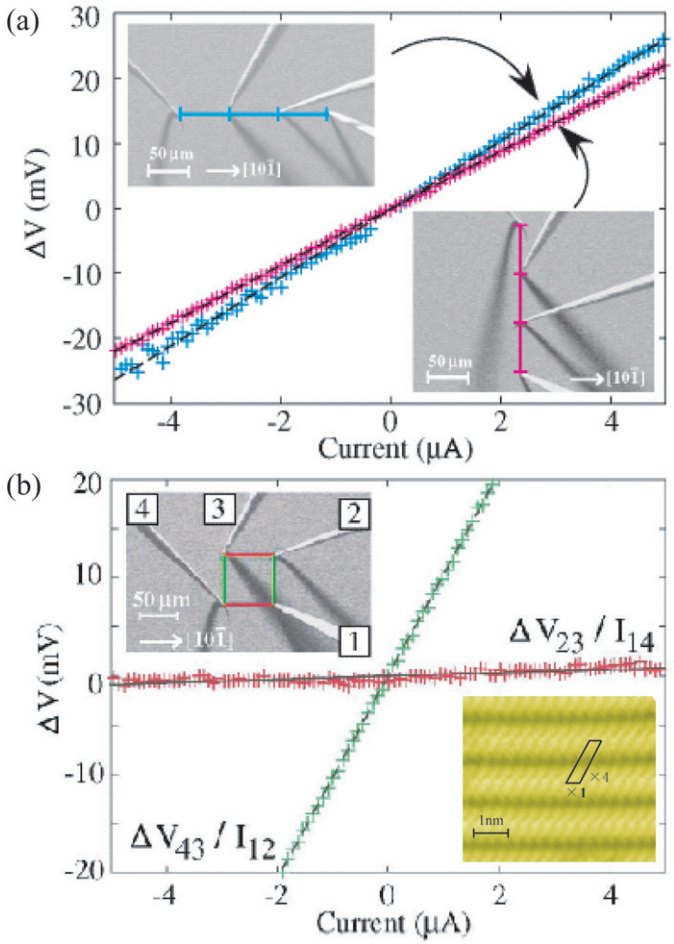

Figure 16. (a) I–V curves from a single-domain Si(111)4 × 1-In surface measured by the linear MFPP method with the probe spacing (distance between two probes) of 60 μm. The blue and red colours correspond to the measurements parallel and perpendicular to the In chains (horizontal direction in the SEM images of insets), respectively. (b) I–V curves measured by the square MFPP method with the probe spacing (a side of the square) of 60 μm. The orange and green colours correspond to the measurements of $\Delta V_{23}/I_{14}$ and $\Delta V_{43}/I_{12}$, respectively. The upper left inset is a SEM image of the probes contacting the sample surface in UHV. The In chains are in horizontal direction in this image. The lower right inset is an STM image of the 4 × 1-In surface, separately taken by a single-tip STM.

substrate conductivity is isotropic). The distinction between figures 16(a) and (b) clearly demonstrates the expectation from equations (11) and (12). It is to be noted that the rotation of the square provides $\sigma_\perp$ and $\sigma_\parallel$ with higher accuracy. Such a rotational MFPP method and the details of the transport research of the 4 × 1-In are described in [40].

We now discuss the value of $\sigma_\parallel$ using the Boltzmann picture in terms of band dispersion and the Fermi surface shown in figure 15(a) [22, 60]. Inserting the corresponding parameters determined by ARPES into equation (1), the conductivity tensor was calculated, and finally we obtained $\sigma_\parallel$ $(=\sigma_{xx}) = 1.4 \times 10^{11} \times \tau_\parallel$ [S/□] and $\sigma_\perp$ $(=\sigma_{yy}) = 7.2 \times 10^9 \times \tau_\perp$ [S/□], where τ_i is the relaxation time in the i direction. By comparing this $\sigma_\parallel$ with the experimentally obtained one, the relaxation time along the In chains is $\tau_\parallel = 5.2(\pm 0.8) \times 10^{-15}$ s. This value is similar to

those of 2D surface layers of the $\sqrt{3}\times\sqrt{3}$-Ag and $\sqrt{21}\times\sqrt{21}$ phases described in the previous section. On the other hand, the value is also similar to that in bulk In crystals, but smaller than that of typical metals by nearly an order of magnitude, calculated by the Drude model [2]. The mean free path along the In chains, estimated from this relaxation time and the group velocity at the Fermi level, is about 3 nm. By assuming $\tau_{\parallel} = \tau_{\perp}$ crudely, one can derive the anisotropy in surface-state conductivity to be 19, which is in reasonable agreement with the experimental one. Conversely, the measured ratio $\sigma_{\parallel}/\sigma_{\perp} \sim 54$ gives a ratio of relaxation time $\tau_{\parallel}/\tau_{\perp} \sim 3$, meaning that the carriers propagate with a longer relaxation time along the In chains.

Thus, the measured 1D anisotropic conductivity is quantitatively consistent with the quasi-1D Fermi surface (Fermi lines). The Boltzmann equation (1) works well for this case as for the case of the $\sqrt{3} \times \sqrt{3}$-Ag surface due to the 'clean' structure, where the density of defects is so low. Another example of a quasi-1D metallic surface, Si(557)-Au [63–66], has a similar anisotropic Fermi surface, but the anisotropy of conductivity is much lower than that of the 4×1-In [34]. This is due to the extremely high density of point defects. This makes the conduction a hopping type, and the temperature dependence of conductivity semiconducting in spite of the metallic Fermi surface.

4. Concluding remarks

In the present paper, we have reviewed Fermi-surface and band-dispersion mappings of metallic atomic layers on semiconductor substrates studied by angle-resolved photoemission spectroscopy, and discussed the close relation to surface transport properties. The first case is for 2D isotropic free-electron-like surface states. The electrical conductivity increases through the change in surface structure, from the $\sqrt{3} \times \sqrt{3}$ to $\sqrt{21} \times \sqrt{21}$, induced by Ag and Au depositions on Si(111)$\sqrt{3} \times \sqrt{3}$-Ag. The conductivity change is well described by evolution of Fermi surfaces (Fermi rings) of these two phases through the Boltzmann equation. The Hall effect during this structural transition is also understood by the electron trajectory on the Fermi surfaces; the majority carriers in the surface states change from electrons to holes. The second case is for quasi-1D free-electron-like surface states. The square-micro-four-point probe method is introduced to measure the anisotropic conductivity of Si(111)4×1-In. The result was quantitatively consistent with those estimated from the Fermi surfaces (Fermi lines). The present research demonstrates that surface atomic layers with their characteristic surface electronic states are a good playground for transport physics, which can be different from other types of low dimensional electronic systems such as in surface inversion layers or at hetero-junctions. Atomically thin low dimensional electronic systems are realized by using surface superstructures, which can enhance quantum effects.

Carrier transport characteristics are sensitive not only to the Fermi surface and band structure, but also to the defects, interference phenomena, and electron correlation effects, especially in reduced dimensions. This is an important and interesting topic, which is not included in the present paper. Actually, high density of defects and disorder in atomic structures of surfaces change the carrier transport from band conduction to hopping-type conductions accompanied by carrier localization phenomena [67, 68]. Collaboration with photoemission and transport measurements is quite fruitful for such quantum transport physics on surfaces.

Acknowledgments

We acknowledge Toru Hirahara, Canhua Liu, Marie D'angelo, Harumo Morikawa, Rei Hobara, and Shinya Yoshimoto, and other former and present members of our laboratory, for the

experiments and calculations. Franz J Himpsel is gratefully acknowledged for giving his valuable comments and providing his experimental data to complete the present paper. This work has been supported by Grants-In-Aid from the Japanese Society for the Promotion of Science and Core Research of Evolutional Science and Technology (CREST) of the Japan Science and Technology Agency (JST).

References

[1] Kittel C 1987 *Quantum Theory of Solids* (New York: Wiley)
[2] Ashcroft N W and Mermin N D 1976 *Solid State Physics* (Philadelphia, PA: Saunders College)
[3] Gruener G 1994 *Density Waves in Solids* (Cambridge: Perseus)
[4] Osterwalder J 1997 *Surf. Rev. Lett.* **4** 391
[5] Hüfner S 1995 *Photoelectron Spectroscopy* (Berlin: Springer)
[6] Osterwalder J 2006 Spin-polarized photoemission *Magnetism: a Synchrotron Radiation Approach* (*Lecture Notes in Physics* vol 697/2006) ed E Beaurepaire, H Bulou, F Scheurer and J-P Kappler (Berlin: Springer) chapter 5, pp 95–120
[7] Schenberg D 1984 *Magnetic Oscillations in Metals* (New York: Cambridge University Press)
[8] Hurd C M 1972 *The Hall Effects in Metals and Alloys* (New York: Plenum)
[9] Tanaka H, Tokumoto M, Ishibashi S, Graf D, Choi E S, Brooks J S, Yasuzuka S, Okano Y, Kobayashi H and Kobayashi A 2004 *J. Am. Chem. Soc.* **126** 10518
[10] Nagai Y, Chiba T, Tang Z, Akahane T, Kanai T, Hasegawa M, Takenaka M and Kuramoto E 2001 *Phys. Rev. Lett.* **87** 176402
[11] Sekiyama A, Iwasaki T, Matsuda K, Saitoh Y, Onuki Y and Suga S 2000 *Nature* **403** 396
[12] Zangwill A 1988 *Physics at Surfaces* (Cambridge: Cambridge University Press)
[13] Plummer E W, Ismail, Matzdorf R, Melechko A V, Pierce J P and Zhang J 2002 *Surf. Sci.* **500** 1
[14] Hasegawa S and Ino S 1992 *Phys. Rev. Lett.* **68** 1192
[15] Hasegawa S and Ino S 1993 *Int. J. Mod. Phys.* B **7** 3817
[16] Hasegawa S, Tong X, Takeda S, Sato N and Nagao T 1999 *Prog. Surf. Sci.* **60** 89
[17] Crain J N and Himpsel F J 2006 *Appl. Phys.* A **82** 431
[18] Hasegawa S, Sato N, Shiraki I, Petersen C L, Bøggild P, Hanssen T M, Nagao T and Grey F 2000 *Japan. J. Appl. Phys.* **39** 3815
[19] Aruga T 2006 *Surf. Sci. Rep.* **61** 283
[20] Ono M, Nishigata Y, Nishio T, Eguchi T and Hasegawa Y 2006 *Phys. Rev. Lett.* **96** 016801
[21] Fukaya Y, Kawasuso A and Ichimiya A 2006 *Surf. Sci.* **600** 3141
[22] Yeom H W, Takeda S, Rotenberg E, Matsuda I, Horikoshi K, Schaefer J, Lee C M, Kevan S D, Ohta T, Nagao T and Hasegawa S 1999 *Phys. Rev. Lett.* **82** 4898
[23] Nagamura N, Matsuda I, Miyata N, Hirahara T, Hasegawa S and Uchihashi T 2006 *Phys. Rev. Lett.* **96** 256801
[24] Matsuda I, Ohta T and Yeom H W 2002 *Phys. Rev.* B **65** 085327
[25] Morikawa H 2004 *PhD Thesis* The University of Tokyo
[26] Neff H-J, Matsuda I, Greber T and Osterwalder J 2001 *Phys. Rev.* B **64** 235415
[27] Hirahara T, Nagao T, Matsuda I, Bihlmayer G, Chulkov E V, Koroteev Y M, Echenique P M, Saito M and Hasegawa S 2006 *Phys. Rev. Lett.* **97** 146803
[28] Hamaguchi T and Taniguchi K 1990 *Physics of Semiconductor Device* (Tokyo: Asakura)
[29] Matsuda I, Hirahara T, Konishi M, Liu C, Morikawa H, D'angelo M, Hasegawa S, Okuda T and Kinoshita T 2005 *Phys. Rev.* B **71** 235315
[30] Yoo K and Weitering H H 2002 *Phys. Rev.* B **65** 115424
[31] Yukawa M, Tatsumi S, Kitagawa H and Iida S 2004 *Japan. J. Appl. Phys.* **43** 8248
[32] Hasegawa Y, Lyo I-W and Avouris P 1996 *Surf. Sci.* **357/358** 32
[33] Heike S, Watanabe S, Wada Y and Hashizume T 1998 *Phys. Rev. Lett.* **81** 890
[34] Okino H, Hobara R, Matsuda I, Kanagawa T and Hasegawa S 2004 *Phys. Rev.* B **70** 113404
[35] Hasegawa S, Shiraki I, Tanabe F, Hobara R, Kanagawa T, Tanikawa T, Matsuda I, Petersen C L, Hansen T M, Bøggild P and Grey F 2003 *Surf. Rev. Lett.* **10** 963
[36] Hasegawa S, Shiraki I, Tanikawa T, Petersen C L, Hansen T M, Bøggild P and Grey F 2002 *J. Phys.: Condens. Matter* **14** 8379
[37] Tanikawa T, Yoo K, Matsuda I, Hasegawa S and Hasegawa Y 2003 *Phys. Rev.* B **68** 113303
[38] Tanikawa T, Matsuda I, Kanagawa T and Hasegawa S 2004 *Phys. Rev. Lett.* **93** 016801
[39] Matsuda I, Ueno M, Hirahara T, Hobara R, Morikawa H, Liu C and Hasegawa S 2004 *Phys. Rev. Lett.* **93** 236801

[40] Kanagawa T, Hobara R, Matsuda I, Tanikawa T, Natori A and Hasegawa S 2003 *Phys. Rev. Lett.* **91** 036805
[41] Hirahara T, Matsuda I, Hobara R, Yoshimoto S and Hasegawa S 2006 *Phys. Rev.* B **73** 235332
[42] Crain J N, Altmann K N, Bromberger C and Himpsel F J 2002 *Phys. Rev.* B **66** 205302
[43] Matsuda I, Morikawa H, Liu C-H, Ohuchi S, Hasegawa S, Okuda T, Kinoshita T, Ottaviani C, Cricenti A, D'angelo M, Soukiassian P and LeLay G 2003 *Phys. Rev.* B **68** 085407
[44] Aizawa H, Tsukada M, Sato N and Hasegawa S 1999 *Surf. Sci.* **429** L509
[45] Tong X, Hasegawa S and Ino S 1997 *Phys. Rev.* B **55** 1310
[46] Lüth H 1995 *Surfaces and Interfaces of Solid Materials* (Berlin: Springer)
[47] Hirahara T, Matsuda I, Ueno M and Hasegawa S 2004 *Surf. Sci.* **563** 191
[48] Hirahara T, Matsuda I and Hasegawa S 2004 *e-J. Surf. Sci. Nanotech.* **2** 141
[49] Pérez-Diestea V, Sánchez-Royob J F, Avilac J, Izquierdoc M, Rocae L, Tejedad A and Asensio M C 2007 *Surf. Sci.* **601** 742
[50] Liu C, Matsuda I, Hobara R and Hasegawa S 2006 *Phys. Rev. Lett.* **96** 036803
[51] Liu C, Yamazaki S, Hobara R, Matsuda I and Hasegawa S 2005 *Phys. Rev.* B **71** 041310(R)
[52] Tong X, Jiang C S, Horikoshi K and Hasegawa S 2000 *Surf. Sci.* **449** 125
[53] Tong X, Ohuchi S, Sato N, Tanikawa T, Nagao T, Matsuda I, Aoyagi Y and Hasegawa S 2001 *Phys. Rev.* B **64** 205316
[54] Liu C, Matsuda I, D'angelo M and Hasegawa S 2006 *Phys. Rev.* B **74** 235420
[55] Zhang H M, Sakamoto K and Uhrberg R I G 2001 *Phys. Rev.* B **64** 245421
[56] Wells J W, Kallehauge J F, Hansen T M and Hofmann Ph 2006 *Phys. Rev. Lett.* **97** 206803
[57] Jiang C-S, Tong X, Hasegawa S and Ino S 1997 *Surf. Sci.* **376** 69
[58] Blood P and Orton J W 1992 *The Electrical Characterization of Semiconductors: Majority Carriers and Electron States* (New York: Academic)
[59] Sze S M 1981 *Physics of Semiconductor Devices* (New York: Wiley) chapter 1
[60] Abukawa T *et al* 1995 *Surf. Sci.* **325** 33
[61] Bunk O *et al* 1999 *Phys. Rev.* B **59** 12228
[62] Wasscher J D 1961 *Phil. Res. Rep.* **16** 301
[63] Altmann K N, Crain J N, Kirakosian A, Lin J-L, Petro-vykh D Y and Himpsel F J 2001 *Phys. Rev.* B **64** 035406
[64] Crain J N, McChesney J L, Zheng F, Gallagher M, Snijders P C, Bissen M, Gundelach C, Erwin S C and Himpsel F J 2004 *Phys. Rev.* B **69** 125401
[65] Losio R, Altmann K N, Kirakosian A, Lin J-L, Petro-vykh D Y and Himpsel F J 2001 *Phys. Rev. Lett.* **86** 4632
[66] Ahn J R, Yeom H W, Yoon H S and Lyo I-W 2003 *Phys. Rev. Lett.* **91** 196403
[67] Yamazaki S, Matsuda I, Okino H, Morikawa H and Hasegawa S 2007 submitted
[68] Matsuda I, Liu C, Hirahara T, Ueno M, Tanikawa T, Kanagawa T, Hobara R, Yamazaki S, Hasegawa S and Kobayashi K 2007 submitted